



A study of gadolinia-doped ceria electrolyte by electrochemical impedance spectroscopy



Lei Zhang ^a, Feng Liu ^a, Kyle Brinkman ^b, Kenneth L. Reifsnider ^c, Anil V. Virkar ^{a,*}

^a Department of Materials Science and Engineering, University of Utah, Salt Lake City, UT 84112, USA

^b Savannah River National Laboratory, Aiken, SC 29808, USA

^c University of South Carolina, Columbia, SC 29208, USA

HIGHLIGHTS

- Measured conductivity of gadolinia-doped ceria by impedance spectroscopy.
- Described transport using an equivalent circuit including leads impedance.
- Determined parameters from maxima and minima of impedance spectra.
- Grain boundary arc can be described accurately by a resistor-capacitor element.

ARTICLE INFO

Article history:

Received 5 June 2013

Received in revised form

5 September 2013

Accepted 7 September 2013

Available online 20 September 2013

Keywords:

Solid oxide fuel cells

Gadolinia-doped ceria

Grain boundary

Impedance spectroscopy

Lead wire impedance

ABSTRACT

Samples of Gd₂O₃-doped CeO₂ (GDC) were fabricated by sintering of powder compacts. Impedance spectra were measured from 400 °C to 675 °C in air by electrochemical impedance spectroscopy (EIS). Above ~500 °C, high frequency arc was not semicircular but could be fitted with a constant phase element (CPE). Above ~625 °C, high frequency arc could not be resolved due to a significant contribution from the inductive load. The impedance spectra were described using a simple equivalent circuit which included the leads/instrument impedance. The leads/instrument impedance was measured over a range of frequencies and temperatures. The high frequency part of the impedance after subtracting leads/instrument impedance could be resolved even at the highest measurement temperature and was described by a semicircle representative of transport across grain boundaries. From these measurements, grain and grain boundary resistivities were determined. The corresponding activation energies were 0.69 eV and 1.11 eV, respectively. The grain boundary capacitance was nearly independent of temperature. The present results show that grain boundary effects can be described by a resistor and a capacitor. Relevant equivalent circuit parameters were obtained from intercepts, maxima and minima in impedance diagrams.

© 2013 Elsevier B.V. All rights reserved.

1. Introduction

Electrochemical Impedance Spectroscopy (EIS) is a technique which measures the response of a sample under an AC stimulus in which the frequency is varied over a wide range. EIS has wide applicability, and has been used for the study of ionic conductors, dielectric materials, semiconductors, solar cells, fuel cells, batteries and corrosion. With improvements in equipment over the years, four types of techniques are typically used to measure and interpret the impedance. They are: AC bridge, Lissajous analysis, phase-

sensitive detection and Fourier analysis. The general approach involves the application of a single frequency input and the measurement of the corresponding current (I) flowing through and the potential drop (V) across the sample. From the measurement of I and V as well as the phase difference over a wide range of frequencies, the real and the imaginary parts of the impedance as a function of frequency can be determined. In 1969, Bauerle in a landmark paper in solid state ionics investigated transport through yttria-stabilized zirconia (YSZ) samples with various applied electrodes and in several atmospheres using electrochemical admittance spectroscopy [1]. Bauerle showed that the measured admittance data could be fitted to semicircles or depressed semicircles in the admittance plane. These semicircles at high frequencies correspond to transport properties through the grain

* Corresponding author. Tel.: +1 801 581 5396; fax: +1 801 581 4816.

E-mail address: anil.virkar@utah.edu (A.V. Virkar).

interiors and across the grain boundaries, and at low frequencies correspond to electrode effects [1]. Bauerle used an equivalent circuit comprising a pure resistor and a pure capacitor in parallel to describe the sample behavior at high frequencies which accurately reproduced the measured spectra. Electrode effects were in part represented using Warburg impedance. Since this original paper, the use of EIS has become commonplace in the study of solid state ionics [2].

The resolution of grain and grain-boundary effects usually requires a high frequency input, often exceeding 100 kHz. It is well known that at high frequencies, there can be a significant contribution from an inductive load, the origin of which lies in the lead wires used to connect to the sample as well as parts of the instrumentation. The effect of the inductive load reflects as an imaginary part of the impedance below the x -axis when the real part is plotted on the positive x -axis and negative of the imaginary part is plotted on the positive y -axis. Thus, in a typical plotting scheme, the capacitive effects appear above the x -axis and the inductive effects appear below the x -axis. When both capacitive and inductive contributions are present to a significant extent, their effects are reflected in the spectra regardless of whether the actual spectra lie above or below the x -axis. Many studies have shown that it is essential to subtract the effects of the leads/instrument before data can be adequately interpreted [2–4]. In a study of $(\text{La}_{1-x}\text{Sr}_x\text{Co}_{1-y}\text{Fe}_y\text{O}_{3-\delta})$ LSCF cathodes using EIS, Esquirol et al. measured the leads/instrument inductance as ~ 125 nH, and the corresponding leads/instrument impedance was subtracted from the raw EIS data [3]. Samson et al. [4] also measured the impedance of an empty cell and subtracted it from the raw data in their study of Sr-doped LaCoO_3 (LSC) cathodes [4]. In many recent studies, however, the approach used has been to ignore that part of the impedance which lies below the x -axis and fit the remaining portion above the x -axis (which is generally not semicircular) using a CPE [5–8]. However, such a procedure does not account for the impedance of the leads/instrument and as such may not represent an accurate measurement of the sample impedance. For example, in a study of electrolyte resistivity, Suzuki et al. did not remove the leads/instrument impedance [5]. They noted that there was a large difference in the measured electrolyte resistance and that expected from separate measurements on bulk samples [5]. They attributed the observed large difference in the electrolyte resistance between the expected value and the measured value to the multilayer structure of their sample [5]. However, the leads/instrument impedance is expected to contain both resistive and inductive contributions, which right-shift the arc leading to an intercept at a larger value (than the sample resistance) on the real axis unless the leads/instrument impedance has been subtracted out. Wang et al. [6] investigated $\text{La}_{0.8}\text{Sr}_{0.2}\text{MnO}_{3-\delta}/\text{Zr}_{0.92}\text{Y}_{0.08}\text{O}_2$ porous electrodes by EIS. In their work the high frequency intercept was equated to the electrolyte and the lead resistance. However, inductive effects of the leads were neglected. Similarly, Zajac et al. investigated the resistivity of doped ceria by EIS [7,8]. In their study, the data below the x -axis were cutoff and the remaining data were analyzed by a CPE as the arcs clearly were not semicircular [7,8].

The use of a CPE generally leads to a better fit to the data than using a capacitor. This of course is not surprising as fitting with a CPE requires two parameters unlike a capacitor, which only needs one parameter. However, the use of a CPE often makes it difficult to offer a unique physical interpretation of the data as the fitting itself may lack uniqueness. In this work, we investigated the conductivity of GDC samples with the objective being the determination of grain and grain boundary ion transport properties. The leads/instrument impedance was separately measured and was subtracted from the data before fitting. The measurements were conducted using the two terminal method. While many studies in the past have

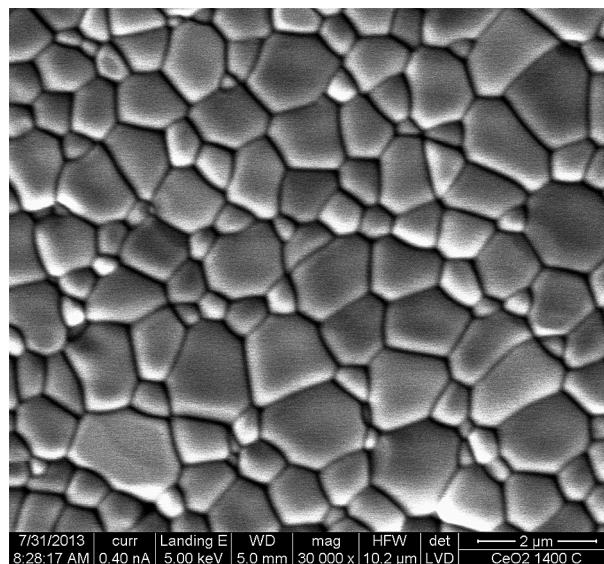


Fig. 1. An SEM image of the GDC sample showing an equiaxed microstructure. The average grain size is ~ 1.1 μm .

emphasized the need to subtract the leads/instrument contribution [2–4], the continual use of procedures in which the inductive part is cutoff and the remainder of the data are fitted using a CPE suggests that revisiting this issue may be of value. The present study also analyzes the data in light of simple equivalent circuits but with the inclusion of the leads/instrument impedance. The present work also attempts to extract relevant parameters of the equivalent circuit from intercepts, maxima and minima in the impedance diagrams.

2. Experimental procedure

Pellets of Gd_2O_3 -doped ceria (GDC) powder of composition 80 mol.% CeO_2 –20 mol.% $\text{GdO}_{1.5}$ were die-pressed and sintered in air at 1400 °C for 2 h. The typical thickness of the pellets was ~ 1.4 mm. Pt paste was applied on both sides of the pellets and they were fired at 800 °C in air for 1 h. Samples of two different electrode geometries (sizes) were used in this study; one set of samples with electrodes 15.8 mm in diameter and the other with electrodes 4.8 mm in diameter.

Impedance spectra were obtained on the samples in air over a range of temperatures between 400 °C and 675 °C in 25° intervals using the two terminal method. The impedance measurements were conducted using Solartron 1260 Frequency Response Analyzer over a frequency (f) range between 0.1 Hz and 1 MHz. Impedance spectra over the same range of temperatures and frequencies were also obtained without the sample (the empty cell) by shorting the two lead wires. This corresponds to the inductive-resistive contribution of the lead wires and the testing setup.

3. Results and discussion

The density of the sintered samples was measured to be 7.0426 g ml^{-1} , which is about 97.37% of theoretical. Fig. 1 shows a scanning electron micrograph (SEM) of a polished and thermally etched sample of a GDC sample. The microstructure is equiaxed and the average grain size is ~ 1.1 μm . Fig. 2 shows an example of how the impedance was measured and interpreted. The corresponding equivalent circuits are shown as insets. Also, an inset in Fig. 2 shows schematics of the two samples used with different electrode areas. For simplicity, the electrodes were also modeled using a parallel R –

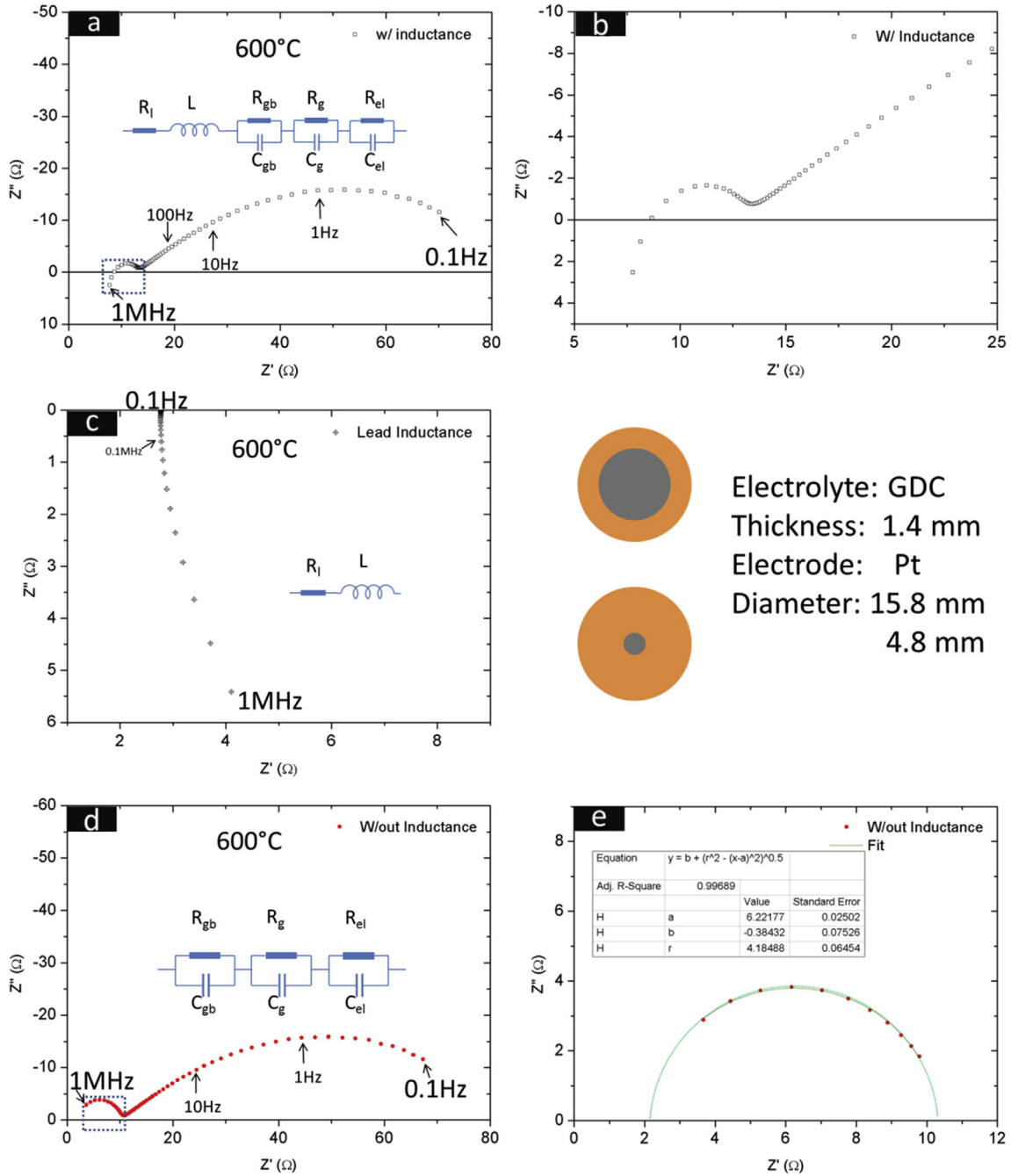


Fig. 2. Experimental approach used for impedance measurements and data interpretation. Inset shows samples with two different electrode areas. (a): Measured impedance of the whole setup, including the sample and the leads/instrument at 600 °C; (b): Enlarged view of the high frequency region in (a); (c): Measured leads/instrument impedance by shorting the leads without the sample; (d): Sample impedance obtained by subtracting the leads/instrument impedance (c) from the measured sample-setup impedance (a); (e): Enlarged view of the boxed part in (d). These data are fitted to a semicircle. From the semicircle, the grain resistance, the grain boundary resistance and the grain boundary capacitance are readily obtained.

C circuit. However, it is clear that the electrodes cannot be represented by this simplified circuit element. Other circuit elements, such as Warburg, and CPE will likely be required to interpret the low frequency data in light of physically realistic mechanisms; e.g. gas diffusion through porous electrodes, adsorption, dissociation, charge transfer. Thus, most of the fitting in this manuscript was restricted to the high frequency part of the impedance spectra even though the analysis includes the electrodes modeled with a parallel R–C circuit. The low frequency part was fitted using a CPE in selected cases for completeness and to obtain a better fit with the data corresponding to the electrode effects. The measured

impedance of the entire setup including the sample at 600 °C is shown in Fig. 2(a). Fig. 2(b) shows an enlarged part of the high frequency region of Fig. 2(a). The impedance of the setup without the sample with the leads shorted is given in Fig. 2(c). The leads/instrument impedance (Fig. 2(c)) was then subtracted from the measured total impedance (Fig. 2(a)). The difference, which should be the sample impedance without the effects of the leads/instrument impedance, is plotted in Fig. 2(d). Finally, the high frequency portion of the impedance from Fig. 2(d) is plotted in Fig. 2(e). The data points in Fig. 2(e) are then fitted using a semicircle. As seen in Fig. 2(e), the data can be fitted very well with a semicircle, which

represents transport across grain boundaries. Fitting with a semi-circle suggests that the grain boundary effects could be adequately represented by a resistor and a capacitor in parallel. Also important to note is that the data point corresponding to the highest frequency of 10^6 Hz (angular frequency, $\omega = 2\pi f = 2\pi \times 10^6$) appears above the x -axis suggesting that the leads inductive-resistive effects appear to have been removed.

Impedance data obtained on a sample with electrodes 15.8 mm in diameter over a temperature range from 400 °C to 675 °C before subtracting the leads/instrument impedance are plotted in Fig. 3(a) and (b). The low frequency regime, as is well known, represents the electrode effects. In this work primarily the high frequency effects were investigated. At low temperatures (below 525 °C) the effects of the leads/instrument impedance are not obvious (although still

present) as the entire measured spectra over the range of frequencies between 0.1 Hz and 1 MHz lie above the x -axis. The near semicircular feature of the high frequency data can be seen in Fig. 3(a). For measurements at 550 °C and above (Fig. 3(b)), the high frequency arc appears as a depressed or a flattened semicircle. At the measurement temperatures of 650 °C and 675 °C, the high frequency arc completely disappears. Also, the leads/instrument inductive effects are clearly seen at higher temperatures, as evidenced by part (or even most) of the measured impedance data lying below the x -axis. The leads/instrument impedance comprising inductive and resistive contributions was found to be weakly dependent on temperature, unlike the sample impedance (resistive part) which exhibits Arrhenius behavior and thus rapidly decreases with increasing temperature. Thus, the effects of the

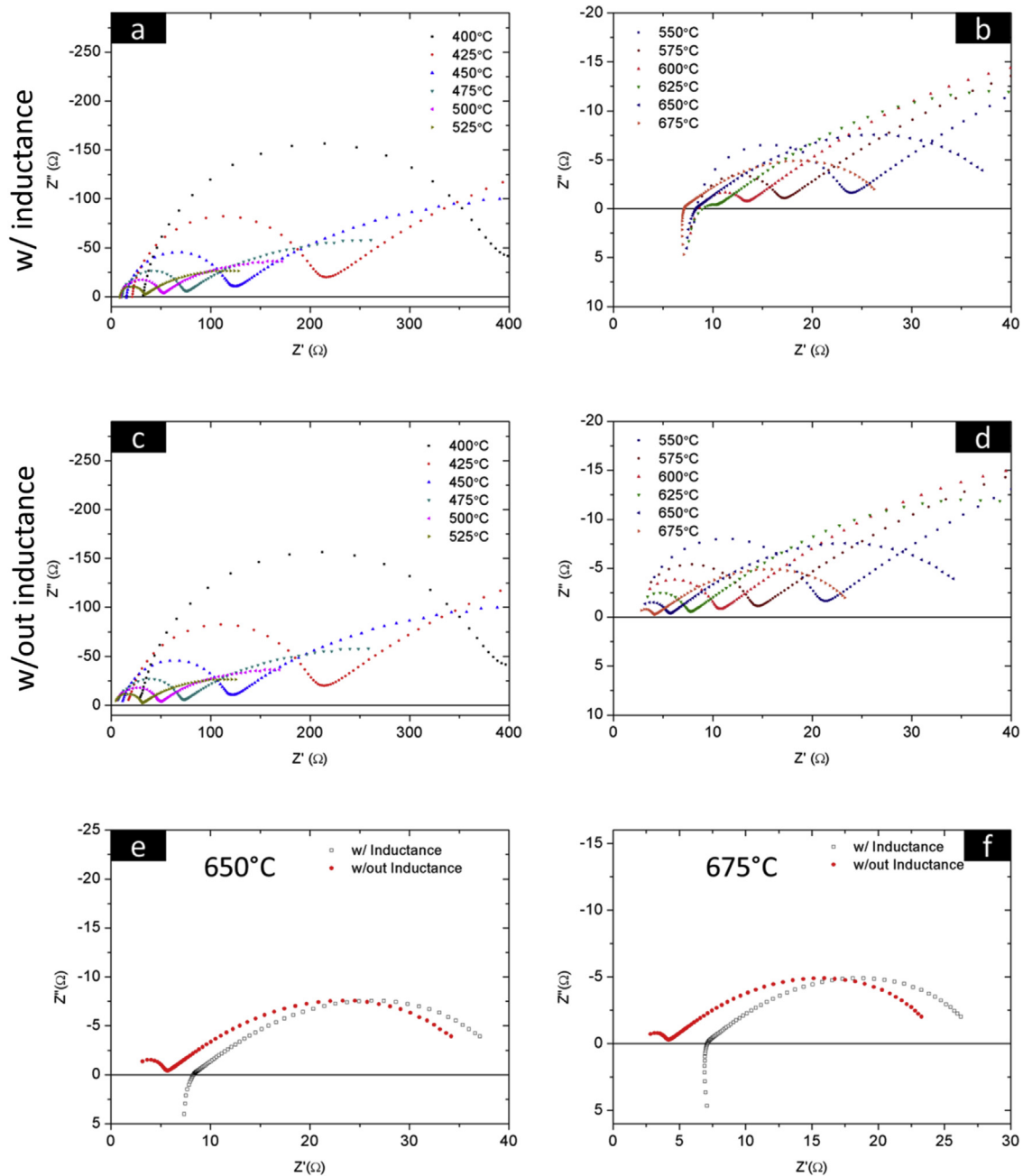


Fig. 3. (a) and (b) are the as-measured impedance spectra for the sample including the leads/instrument impedance over the same temperature range; (c) and (d) are the corresponding impedance spectra after subtracting the leads/instrument impedance over the same temperature range; (e) and (f) compare the plots with and without the leads/instrument effects at 650 °C and 675 °C, respectively. Note that once the leads/instrument effects are subtracted out, the high frequency arcs are resolved and that they are semicircular in shape.

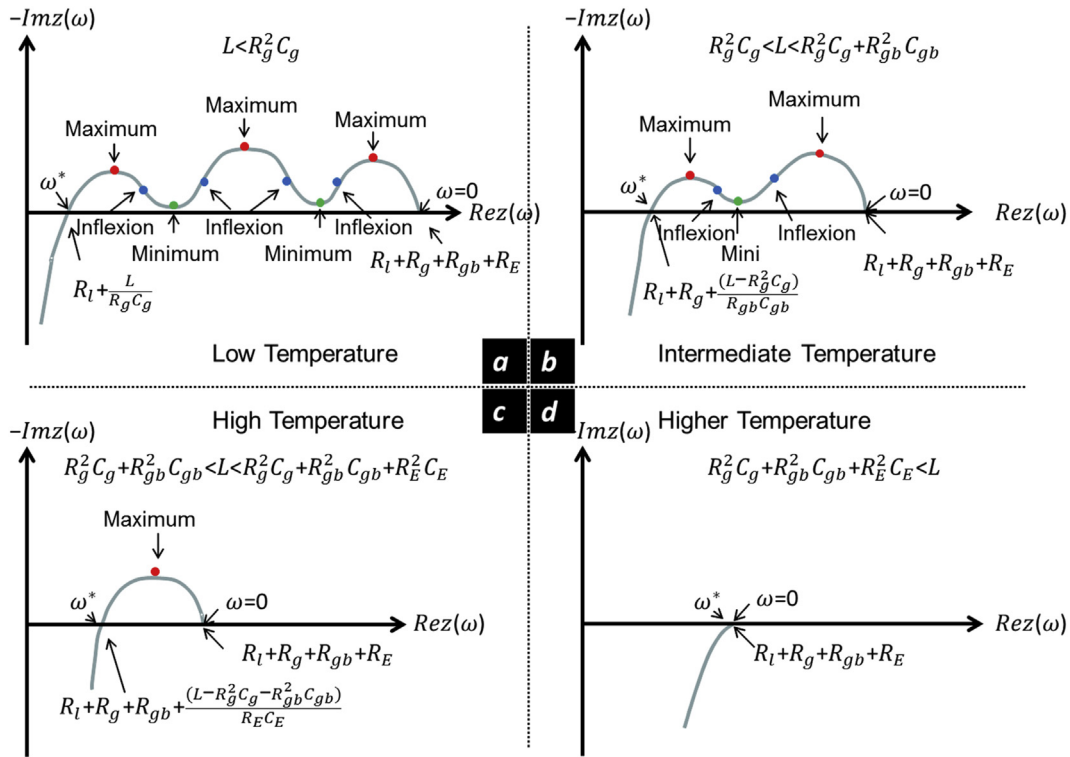


Fig. 4. (a): A schematic showing the expected impedance plot at a low temperature when grain, grain boundary and electrode effects can be described by parallel R–C circuits and when the time constants for the three processes are sufficiently far apart. The impedance plot exhibits 3 maxima, 2 minima, and 4 inflexion points. Typically, the inflexion points are located very close to the minima. The real part corresponding to $\omega \rightarrow 0$ is given by $R_l + R_g + R_{gb} + R_E$. The real part corresponding to the high frequency intercept is equal to $Re z(\omega^*) = R_l + L/R_g C_g$. (b): A schematic showing the expected impedance plot at an intermediate temperature when grain, grain boundary and electrode effects can be described by parallel R–C circuits and when the time constants for the three processes are sufficiently far apart. The impedance plot exhibits 2 maxima, 1 minimum, and 2 inflexion points. The real part corresponding to $\omega \rightarrow 0$ is given by $R_l + R_g + R_{gb} + R_E$. The real part corresponding to the high frequency intercept is given by $Re z(\omega^*) = R_l + R_g + (L - R_g^2 C_g)/R_{gb} C_{gb}$. (c): A schematic showing the expected impedance plot at a high temperature when grain, grain boundary and electrode effects can be described by parallel R–C circuits and when the time constants for the three processes are sufficiently far apart. The impedance plot exhibits 1 maximum. The real part corresponding to $\omega \rightarrow 0$ is given by $R_l + R_g + R_{gb} + R_E$. The real part corresponding to the high frequency intercept is given by $Re z(\omega^*) = R_l + R_g + R_{gb} + (L - R_g^2 C_g - R_{gb}^2 C_{gb})/R_E C_E$. (d): A schematic showing the expected impedance plot at an even higher temperature when grain, grain boundary and electrode effects can be described by parallel R–C circuits and when the time constants for the three processes are sufficiently far apart. The impedance plot exhibits no maxima, no minima, and no inflexion points. The real part corresponding to $\omega \rightarrow 0$ is given by $R_l + R_g + R_{gb} + R_E$. There is no arc above the x-axis. Thus, the $\omega^* = \omega = 0$.

leads/instrument impedance become more significant relative to the sample at higher temperatures, which is of course well known.

Fig. 3(c) and (d) shows the same data, respectively, from Fig. 3(a) and (b), but from which the leads/instrument impedance has been subtracted. Thus, the data in Fig. 3(c) and (d) represents the sample impedance without any leads/instrument effects. All high frequency arcs now appear perfectly semicircular. Also, no data points lie below the x-axis showing that the effects of the leads/instrument have been subtracted out. Also note that even at the highest measurement temperature of 675 °C, the high frequency semicircular arc is fully resolved and is clearly visible. Fig. 3(e) and (f) respectively shows the measured data at 650 °C and 675 °C, in which the plots include data with and without leads/instrument effects. As clearly seen, the semicircle representing the grain resistance, the grain boundary resistance, and the grain boundary capacitance can be clearly resolved once the leads/instrument impedance is subtracted, unlike the raw data in which no high frequency arcs can be seen.

For the high frequency data, such as at 1 MHz noted in Fig. 3(e) and (f), the change in impedance after subtracting the leads/instrument impedance consists of both the real part and the imaginary part corresponding to the leads/instrument resistance and the leads/instrument inductance. With decreasing frequency, the effect of the leads/instrument inductance decreases, but naturally the resistive (ohmic) contribution remains the same. At very low frequencies, such as at a few Hz and below, the inductive part essentially disappears and only the real part from the leads/

instrument resistance remains. Electrolyte transport properties are reflected typically in the high frequency EIS data, so the leads/instrument impedance needs to be accounted for. Information concerning the electrode kinetics is typically reflected in the low to intermediate frequency EIS data, and thus one generally needs to correct only for the ohmic part. Therefore, no matter whether the electrolyte or the electrodes are investigated in an EIS study, subtraction of the leads/instrument impedance is necessary when the two terminal method is used.

Analysis of impedance spectra including electrode, grain boundary and grain effects: The most general case but assuming simple resistor-capacitor elements is examined in what follows. At very high frequencies, the effects of grain resistance, R_g , and grain capacitance, C_g , may become observable. This will likely be the case at low temperatures when $R_g^2 C_g$ is large in relation to (or comparable to) the leads/instrument inductance, L . The real and the imaginary parts of the impedance are given respectively by

$$Re z(\omega) = R_l + \frac{R_g}{(1 + R_g^2 \omega^2 C_g^2)} + \frac{R_{gb}}{(1 + R_{gb}^2 \omega^2 C_{gb}^2)} + \frac{R_E}{(1 + R_E^2 \omega^2 C_E^2)} \quad (1)$$

where R_l is the leads/instrument resistance and

$$\text{Im}z(\omega) = \omega \left[L - \frac{R_g^2 C_g}{(1 + R_g^2 \omega^2 C_g^2)} - \frac{R_{gb}^2 C_{gb}}{(1 + R_{gb}^2 \omega^2 C_{gb}^2)} - \frac{R_E^2 C_E}{(1 + R_E^2 \omega^2 C_E^2)} \right] \quad (2)$$

Equation (2) shows that $\text{Im} z(\omega) \rightarrow 0$ as $\omega \rightarrow 0$. The corresponding real part is given by

$$\text{Re}z(\omega = 0) = R_1 + R_g + R_{gb} + R_E \quad (3)$$

In what follows, we will assume that over some range of temperatures

$$L < R_g^2 C_g + R_{gb}^2 C_{gb} + R_E^2 C_E \quad (4)$$

Thus, there is a range of frequencies over which an arc exists above the x -axis in the plot of $-\text{Im} z(\omega)$ vs. $\text{Re} z(\omega)$, and at a sufficiently high angular frequency, we have

$$\left[L - \frac{R_g^2 C_g}{(1 + R_g^2 \omega^2 C_g^2)} - \frac{R_{gb}^2 C_{gb}}{(1 + R_{gb}^2 \omega^2 C_{gb}^2)} - \frac{R_E^2 C_E}{(1 + R_E^2 \omega^2 C_E^2)} \right] = 0 \quad (5)$$

If, however, $L > R_g^2 C_g + R_{gb}^2 C_{gb} + R_E^2 C_E$, no arc is observed above the x -axis. Such a situation can occur in a given system above some temperature since typically, R_g , R_{gb} and R_E all exhibit an Arrhenius behavior and thus decrease with increasing temperature while L is generally temperature independent. Equation (5) is a cubic equation in ω^2 and should have one real positive root, which we will denote by ω^* . For angular frequencies above ω^* the $\text{Im} z(\omega) > 0$, and will appear below the x -axis. Over the angular frequency range $\omega^* > \omega > 0$, the $\text{Im} z(\omega) < 0$ and will appear as an arc above the x -axis. The general shape of the plot with $-\text{Im} z(\omega)$ on the y -axis and $\text{Re} z(\omega)$ on the x -axis is shown in Fig. 4(a).

The general shape of the impedance spectra over the range $\omega^* > \omega > 0$ is characterized by: (a) three maxima, (b) two minima, and (c) four inflexion points. These correspond to: (a) $d(-\text{Im} z(\omega))/d(\text{Re} z(\omega)) = 0$, $d^2(-\text{Im} z(\omega))/d(\text{Re} z(\omega))^2 < 0$; (b) $d(-\text{Im} z(\omega))/d(\text{Re} z(\omega)) = 0$, $d^2(-\text{Im} z(\omega))/d(\text{Re} z(\omega))^2 > 0$; and (c) $d^2(-\text{Im} z(\omega))/d(\text{Re} z(\omega))^2 = 0$. As long as $d(\text{Re} z(\omega))/d\omega$ is finite and nonzero, the above conditions may also be given as: (a) $d(-\text{Im} z(\omega))/d\omega = 0$, $d^2(-\text{Im} z(\omega))/d\omega^2 < 0$; (b) $d(-\text{Im} z(\omega))/d\omega = 0$, $d^2(-\text{Im} z(\omega))/d\omega^2 > 0$; and (c) $d^2(-\text{Im} z(\omega))/d\omega^2 = 0$. Depending upon the relative values of the various parameters and the range of frequencies, it is possible to have: (i) Three maxima, two minima, and four inflexion points; (ii) Two maxima, one minimum, and two inflexion points; (iii) One maximum, and one or two inflexion points; (iv) One maximum; (v) No maxima, no minima, and no inflexion points. This last situation corresponds to the case where the entire spectra appear below the x -axis. In what follows, we will first examine some limiting cases.

Case I. Low Temperature: Suppose the temperature is sufficiently low such that

$$L < R_g^2 C_g \quad (6)$$

(and thus also naturally $L < R_g^2 C_g + R_{gb}^2 C_{gb} + R_E^2 C_E$). We also assume that $R_E C_E \gg R_{gb} C_{gb} \gg R_g C_g$, which are the time constants respectively for the electrode, the grain boundary and the grain transport processes. This may lead to distinct arcs corresponding to electrode, grain boundary, and grain effects. The corresponding observed behavior will be that shown in Fig. 4(a). If however the

time constants are not sufficiently different for the three processes, overlapping spectra are expected and three distinct arcs may not be observed. When $\omega = 0$, the corresponding real part of the impedance is given by $\text{Re} z(\omega = 0) = R_1 + R_g + R_{gb} + R_E$, which is the same as Equation (3). Assuming $R_E C_E \gg R_{gb} C_{gb} \gg R_g C_g$, at sufficiently high values of the angular frequency,

$$\text{Im}z(\omega) \approx \omega \left[L - \frac{R_g^2 C_g}{(1 + R_g^2 \omega^2 C_g^2)} \right] \quad (7)$$

in which we have substituted $R_E C_E \omega \gg R_{gb} C_{gb} \omega \gg 1$. Thus, the corresponding ω (which we will denote ω^*) at which $\text{Im} z(\omega) = 0$ is given by

$$\left[L - \frac{R_g^2 C_g}{(1 + R_g^2 \omega^{*2} C_g^2)} \right] = 0 \quad (8)$$

The ω^* is thus the angular frequency at which capacitive and inductive parts of the impedance are equal in magnitude (but opposite in sign).

Thus,

$$\omega^* = \frac{1}{R_g C_g} \sqrt{\frac{R_g^2 C_g - L}{L}} \quad (9)$$

The corresponding real part of the impedance is given by

$$\text{Re}z(\omega^*) = R_1 + \frac{L}{R_g C_g} \quad (10)$$

At angular frequencies $\omega > \omega^*$ given by Equation (9), the impedance spectra appear below the x -axis. We expect the general expression for $-\text{Im} z(\omega)$ to be described by Equation (2) and the plot of $-\text{Im} z(\omega)$ vs. $\text{Re} z(\omega)$ given by Fig. 4(a). Such a plot thus should exhibit three maxima, two minima and four inflexion points, assuming the frequency range is wide enough.

Case II. Intermediate temperature range: At some temperature (higher than for Case I), the relative value of the leads/instrument inductance may be such that $R_g^2 C_g < L < R_g^2 C_g + R_{gb}^2 C_{gb}$. The point $\omega = 0$ gives the real part, the same as Equation (3), and $-\text{Im} z(0) = 0$. As the angular frequency is increased, there will be a frequency at which

$$\text{Im}z(\omega^*) = \omega^* \left[L - R_g^2 C_g - \frac{R_{gb}^2 C_{gb}}{(1 + R_{gb}^2 \omega^{*2} C_{gb}^2)} \right] = 0 \quad (11)$$

in which we have substituted $R_E C_E \omega \gg 1 \gg R_g C_g \omega$. The corresponding ω^* is given by

$$\omega^* = \frac{1}{R_{gb} C_{gb}} \sqrt{\frac{R_{gb}^2 C_{gb} + R_g^2 C_g - L}{L - R_g^2 C_g}} \quad (12)$$

and the corresponding real part of the impedance is given by

$$\text{Re}z(\omega^*) = R_1 + R_g + \frac{(L - R_g^2 C_g)}{R_{gb} C_{gb}} \quad (13)$$

At angular frequencies higher than ω^* given by Equation (12), the impedance spectra appear below the x -axis. The plot of $-\text{Im} z(\omega)$ vs. $\text{Re} z(\omega)$ may likely exhibit two maxima, one minimum, and two inflexion points. Fig. 4(b) shows a schematic of the anticipated EIS spectra at an intermediate temperature.

We will now examine the minimum in $-\text{Im } z(\omega)$ shown in Fig. 4(b). The $\text{Im } z(\omega)$ over the range of frequencies may be approximately given by

$$\text{Im}z(\omega) = \omega \left[L - R_g^2 C_g - R_{gb}^2 C_{gb} - \frac{R_E^2 C_E}{1 + R_E^2 \omega^2 C_E^2} \right] \quad (14)$$

in which we have substituted $R_g^2 \omega^2 C_g^2 \ll R_{gb}^2 \omega^2 C_{gb}^2 \ll 1$. The minimum in $-\text{Im } z(\omega)$ is given by

$$\frac{d\text{Im}z(\omega)}{d\omega} = L - R_g^2 C_g - R_{gb}^2 C_{gb} + \frac{1}{C_E \omega^2} = 0 \quad (15)$$

which gives

$$\omega_{\min}^2 = \frac{1}{C_E (R_g^2 C_g + R_{gb}^2 C_{gb} - L)} \quad (16)$$

It is easily verified that Equation (16) corresponds to a minimum in $-\text{Im } z(\omega)$. Substitution for ω_{\min}^2 into the equation for the real part of the impedance gives the real part of the impedance corresponding to the minimum by

$$\begin{aligned} \text{Re}z(\omega_{\min}) = R_1 + R_g + & \frac{R_{gb} C_E (R_g^2 C_g + R_{gb}^2 C_{gb} - L)}{C_E (R_g^2 C_g + R_{gb}^2 C_{gb} - L) + R_{gb}^2 C_{gb}^2} \\ & + \frac{R_E C_E (R_g^2 C_g + R_{gb}^2 C_{gb} - L)}{C_E (R_g^2 C_g + R_{gb}^2 C_{gb} - L) + R_E^2 C_E^2} \end{aligned} \quad (17)$$

Thus the arc length between $\omega = 0$ and $\omega = \omega_{\min}$ is given by

$$\begin{aligned} \text{Re}z(\omega = 0) - \text{Re}z(\omega = \omega_{\min}) = & \frac{R_{gb}^3 C_{gb}^2}{C_E (R_g^2 C_g + R_{gb}^2 C_{gb} - L) + R_{gb}^2 C_{gb}^2} \\ & + \frac{R_E^3 C_E^2}{C_E (R_g^2 C_g + R_{gb}^2 C_{gb} - L) + R_E^2 C_E^2} \end{aligned} \quad (18)$$

Note that only if $R_E^2 C_E^2 \gg (R_g^2 C_g + R_{gb}^2 C_{gb} - L) C_E \gg R_{gb}^2 C_{gb}^2$, Equation (18) reduces to R_E as the arc length.

Case III. Higher temperature range: At some higher temperature (higher than for Case II), the relative value of the leads/instrument inductance may be such that

$$R_g^2 C_g + R_{gb}^2 C_{gb} < L < R_g^2 C_g + R_{gb}^2 C_{gb} + R_E^2 C_E$$

The point $\omega = 0$ still gives the real part the same as Equation (3) and the $-\text{Im } z(0) = 0$. As the angular frequency is increased, there will be a frequency at which

$$\text{Im}z(\omega^*) = \omega^* \left[L - R_g^2 C_g - R_{gb}^2 C_{gb} - \frac{R_E^2 C_E}{1 + R_E^2 \omega^{*2} C_E^2} \right] = 0 \quad (19)$$

in which we have substituted $R_g C_g \omega \ll R_{gb} C_{gb} \omega \ll 1$. The corresponding ω^* is given by

$$\omega^* = \frac{1}{R_E C_E} \sqrt{\frac{R_E^2 C_E + R_{gb}^2 C_{gb} + R_g^2 C_g - L}{L - R_g^2 C_g - R_{gb}^2 C_{gb}}} \quad (20)$$

The corresponding real part is given by

$$\text{Re}z(\omega^*) = R_1 + R_g + R_{gb} + \frac{L - R_g^2 C_g - R_{gb}^2 C_{gb}}{R_E C_E} \quad (21)$$

A plot of $-\text{Im } z(\omega)$ vs. $\text{Re } z(\omega)$ will likely exhibit one maximum, no minima, and no inflexion points. Fig. 4(c) shows a schematic.

Case IV. An even higher temperature range: Suppose the leads/instrument inductance, L , is such that

$$L > R_g^2 C_g + R_{gb}^2 C_{gb} + R_E^2 C_E \quad (22)$$

a situation that may occur at rather high temperatures. In such a case, the entire impedance curve lies below the x -axis – no arc is seen above the x -axis. When $\omega = 0$, the $-\text{Im } z(\omega) = 0$ and the corresponding real part of the impedance is given by

$$\text{Re}z(\omega = 0) = R_1 + R_g + R_{gb} + R_E \quad (23)$$

which is the same as Equation (3). Also, therefore, in this case $\omega^* = 0$. Thus, assuming data can be realistically obtained at very low frequencies ($\omega \rightarrow 0$), the corresponding intercept on the x -axis corresponds to the total resistance including all components regardless of the relative values of the various parameters. Fig. 4(d) shows a schematic. Thus, in the event that with increasing temperature the arc above the x -axis completely disappears, the corresponding intercept as $\omega \rightarrow 0$ is still the total resistance.

Interpretation of the experimental results using the preceding analysis: In light of the preceding analysis, we will now examine the impedance spectra in Fig. 3(a) and (b) obtained on a GDC sample measured over a temperature range from 400 °C to 675 °C in air and over a frequency (f) range from 0.1 Hz to 1 MHz using the two terminal method. Up to 525 °C, almost the entire spectra are above the x -axis. This means up to 525 °C, the ω^* is greater than the maximum angular frequency at which measurements were made; that is for temperatures up to 525 °C, $\omega^* > 2\pi \times 10^6$. Above 525 °C, part of the measured spectra lie below the x -axis, and thus above 525 °C, $\omega^* < 2\pi \times 10^6$. The spectra also show that up to 600 °C, a distinct high frequency arc can be seen. Thus, over the range of frequencies investigated, between about 425 °C and 600 °C, the observed spectra contain one maximum, one minimum, and two inflexion points. Also therefore, over the range of experimental parameters (both the sample and the testing parameters), the low temperature case (Case I, Fig. 4(a)) is not observed. Over the temperature range from 400 °C to 600 °C, the observed spectra correspond to Case II (Fig. 4(b)), in which $R_g^2 C_g < L < R_g^2 C_g + R_{gb}^2 C_{gb}$. Spectra at 650 °C and 675 °C do not exhibit a high frequency arc.

Over the temperature range from 400 °C to 600 °C, the high frequency arc is clearly visible. As stated earlier, the highest angular frequency at which measurements were made was $\omega_{\max} = 2\pi \times 10^6 \text{ s}^{-1}$ in all experiments. Over the temperature range from 400 °C to 450 °C the entire spectra are above the x -axis. This means the corresponding $\omega^* > \omega_{\max}$. The ω^* thus may be obtained by extrapolation. Also, extrapolation to the x -axis gives the corresponding real part which is identified with $\text{Re}z(\omega^*) = R_1 + R_g + (L - R_g^2 C_g) / R_{gb} C_{gb}$, namely Equation (13). Over the temperature range 450 °C–600 °C, the high frequency arc can be seen and at the same time some of the data lie below the x -axis. In these cases, $\omega^* < \omega_{\max}$. The real part of the impedance corresponding to ω^* is again given by Equation (13).

At 650 °C and 675 °C, no high frequency arc is observed. This temperature thus corresponds to the range $R_g^2 C_g + R_{gb}^2 C_{gb} < L < R_g^2 C_g + R_{gb}^2 C_{gb} + R_E^2 C_E$. This corresponds to Case III, Fig. 4(c). The real part of the impedance corresponding to ω^* is thus given by $\text{Re}z(\omega^*) = R_1 + R_g + R_{gb} + (L - R_g^2 C_g - R_{gb}^2 C_{gb}) / R_E C_E$ which is

Table 1
Fitting parameters used to fit simulation spectra in Fig. 3. Parameters are given only up to a temperature of 600 °C as no minimum was observed at higher temperatures.

T (°C)	L (nH)	R _l (Ω)	R _g (Ω)	C _g (F)	R _{gb} (Ω)	C _{gb} (nF)	τ _{gb} (μS)	Set value		τ _e (S)
								R _E (Ω)	C _E (mF)	
400	882	3.68	28.4	0	364	34.7	12.6	2.6 k	0.81	2.13
450	874	3.78	10.8	0	107	33.3	3.56	577	1.86	1.07
500	871	3.88	4.69	0	41	30.9	1.26	229	4	0.915
550	866	4.01	2.37	0	18.4	34.5	0.634	141	5.52	0.776
600	861	4.1	2.06	0	8.32	38.2	0.318	82.5	7.09	0.585

T (°C)	Simulated	Measured	ω (kHz)	Simulated value		ΔR _E (%)	ΔC _E (%)
	Re(Z) (Ω)	Re(Z) (Ω)		R _E (Ω)	C _E (mF)		
400	396	413	0.52	2.6 k	0.81	−1.5	−0.19
450	122	129	1.19	584	1.86	1.22	0.29
500	49.6	51.4	2.21	232	4.01	1.56	0.09
550	24.7	24.8	4.1	139	5.52	−1.2	−0.15
600	14.5	13.4	8.89	83.6	7.1	1.34	0.04

Equation (21). In view of the fact that the electrode effects cannot be adequately described by a parallel $R_E - C_E$ circuit element, the applicability of Equation (21) to the present data may only be treated as being approximate.

Simulation and data fitting: Experimental results shown in Fig. 3(a) and (b) were analyzed using the simple equivalent circuit in which electrode, grain boundary and grain processes are described using parallel $R - C$ circuits. The fitting of the electrode effects by a parallel $R_E - C_E$ circuit is not accurate since clearly the electrode arc is not semicircular. The primary focus of the fitting, however, is the high frequency regime – namely grain boundary and grain. Also, it was assumed that the grain capacitance C_g is very small over the range of frequencies and thus can be set to zero (actually, this means $L \gg R_g^2 C_g$). This assumption, however, is not expected to be valid at lower temperatures. Thus, the simulation does not include the low temperature Case I, which was not observed in the present work over the range of temperatures and frequencies investigated.

Table 1 gives the experimental values and the fitted values of the various parameters over a range of temperatures between 400 °C and 700 °C in 50 °C intervals. Experimental data in Fig. 3 correspond to one minimum below 600 °C (the schematic corresponding to Fig. 4(b)). This minimum corresponds to Case II, the intermediate temperature case. The corresponding ω_{\min}^2 is given by Equation (16). Table 1 shows the values of L , R_l , R_g , R_{gb} , C_{gb} , R_E and C_E (with C_g assumed to be zero). Note that the L is essentially independent of temperature (it very slightly decreases with increasing temperature) and R_l slightly increases with increasing temperature. Table 1 also lists ω_{\min} over the temperature range from 400 °C to 600 °C. At 650 °C and above, which corresponds to Case III, no high frequency arc is observed, and $\omega_{\min}^2 < 0$, which means no minimum exists (that is at and above 650 °C, $L > R_{gb}^2 C_{gb}$). The values of the various parameters in Table 1 indeed show that at and above 650 °C, $L > R_{gb}^2 C_{gb}$. The estimated values of R_E and C_E from the simulation are very close to the set values of R_E and C_E .

Fig. 5(a) through (f) is the simulated EIS spectra over the temperature range 400 °C–650 °C in 50 °C intervals and over the frequency range from 0.1 Hz to 10^6 Hz. Also shown in each of the figures (from Fig. 5(a) through (e)) is an inset corresponding to the minimum in $-\text{Im } z(\omega)$ (corresponding to ω_{\min}). From each of the minima, the corresponding $\text{Re } z(\omega_{\min})$ was estimated, also shown in the insets. The experimental values of $\text{Re } z(\omega_{\min})$ were determined from the measured spectra given in Fig. 3(a) and (b). These values are also listed in Table 1. The agreement between the two is very good. In Fig. 5(f), which shows spectra at 650 °C, no high frequency

arc is observed. The inset shows enlarged view of the data near the intersection with the x -axis.

Table 1 also lists the values of R_g and R_{gb} as a function of temperature. The R_g varies between $\sim 28.8 \Omega$ at 400 °C and $\sim 2.04 \Omega$ at 575 °C. Over the same range of temperatures, the R_{gb} varies between $\sim 364 \Omega$ and 11.94Ω . These results show that even at 575 °C, the R_{gb} is greater than R_g . Above about 600 °C, the R_g appears to be independent of temperature. But this observation is related to inaccuracies in the measurements (errors involved in the removal of the leads impedance). It is the expectation that both R_g and R_{gb} will continue to decrease with increasing temperature. In order to improve the accuracy of measurements, one would need to use samples of larger total resistance (smaller electrode area and/or thicker samples) compared to the ones used in the present work. The R_{gb} continues to decrease with increasing temperature. There likely are greater uncertainties in both values above 600 °C. The observation, however, that even at a temperature as high as 650 °C the R_{gb} is comparable to (or greater than) R_g implies that the absence of a high frequency arc in the measured spectra (when not corrected for the leads/instrument impedance) cannot be interpreted to mean that the grain boundary resistance is negligible compared to the grain resistance.

Table 1 shows that the C_{gb} is essentially independent of temperature over the range 400 °C–600 °C, and seems to increase slightly above 600 °C. This apparent increase in C_{gb} at higher temperatures is again related to the inaccuracies in the measurements and samples of appropriate geometries will be required to obtain accurate values of all three parameters, namely R_g , R_{gb} and C_{gb} . The C_{gb} is expected to be essentially independent of temperature over a very wide range since impurity and dopant profiles near the grain boundaries and the associated space charge effects are practically frozen in from the sintering temperature [9–12].

Electrode parameters: As stated earlier, the electrode effects cannot be accurately described by a parallel $R-C$ circuit element given the nature of many complex processes that occur at the electrodes, such as gas phase diffusion through porous electrodes, adsorption and dissociation of O_2 molecules, electron transfer corresponding to the oxygen reduction reaction (ORR) as well as the oxygen ion oxidation reaction (the reverse of ORR), and the incorporation/extraction of O^{2-} at the electrode/electrolyte interface (typically at three phase boundaries, TPBs). However, if electrode effects can be adequately described in any given system by a parallel $R-C$ circuit, the present work shows that it may be possible to obtain both R_E and C_E from the minimum in $-\text{Im } z(\omega)$ when it is impractical to make measurements at ultra-low angular frequencies. Table 1 compares the estimated values of R_E and C_E from the minima in $-\text{Im } z(\omega)$ with those used in the simulations. It is observed that the error in R_E is typically less than 2% and that in C_E is much lower. In the present work, measurements were made at frequencies ≥ 0.1 Hz, which precluded the estimation of the R_E from the arc length. Thus, the values of electrode parameters, namely R_E and C_E , were obtained from the minimum, especially at lower temperatures. An examination of Fig. 3(a) and (b) shows that if the low frequency arcs are extrapolated to zero angular frequency (to the x -axis), the values obtained for R_E are on the same order of magnitude as selected for the simulation and the ones estimated from the minima in $-\text{Im } z(\omega)$. Although these estimates are not expected to be accurate, some conclusions may nevertheless be drawn from the values obtained for R_E and C_E .

Over the temperature range from 400 °C to 600 °C, the R_E varies between 2620 Ω and 82.45 Ω , or by a factor of ~ 31 , clearly showing that the overall electrode reaction exhibits a strong temperature dependence. It is well known that the reaction of charge transfer, described by such models as the Butler–Volmer equation, is usually thermally activated, and a strong temperature dependence is to be

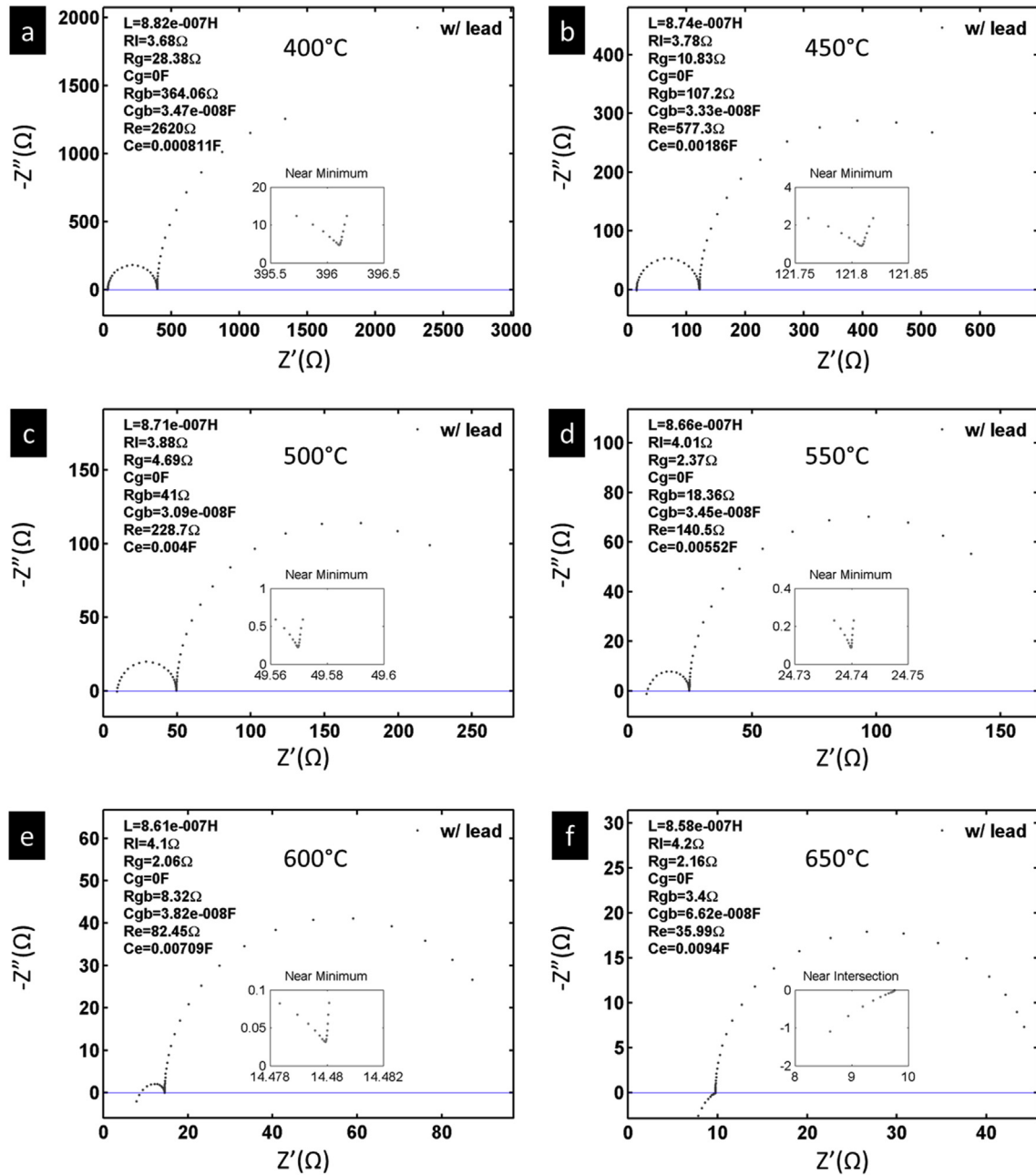


Fig. 5. Simulated impedance spectra: (a): 400 °C, (b): 450 °C, (c): 500 °C, (d): 550 °C, (e): 600 °C, and (f): 650 °C.

expected, as observed here. The other temperature-dependent processes which affect R_E include gas phase adsorption and dissociation. Indeed, in the original landmark paper by Bauerle [1], the resistance describing the electrode reaction exhibited a thermally activated behavior. Over the same range of temperatures, the electrode capacitance, C_E varies from 8.11×10^{-4} f at 400 °C to 7.09×10^{-3} f at 600 °C. That is the C_E varies by ~ 9 times. Such a large variation in C_E is consistent with the nature of processes that occur at the electrolyte/electrode interface is that of O_2 adsorption and its dissociation. This determines the surface coverage of adsorbed O_2 (or O) and thus would dictate the overall charge transfer reaction. The temperature dependence of the adsorption and dissociation processes would thus be expected to affect the C_E resulting in a temperature dependence of C_E . Thus, unlike the grain boundary

capacitance, C_{gb} , which is expected to be essentially temperature-independent, the electrode capacitance, C_E , would likely exhibit temperature dependence. As stated earlier, the description of electrode effects by a parallel resistor-capacitor circuit element is an over simplification. In principle, however, it should be possible to develop similar analysis as given here but with a more representative circuit element for the electrodes (e.g. CPE). If this can be done, it may be possible to estimate the electrode parameters from the analysis of the minima in $-\text{Im} Z(\omega)$ vs. ω ; that is from ω_{\min} .

The analysis given here assumes that the time constants for the three processes, namely, grain, grain boundary and electrode, are sufficiently far apart so that impedance spectra should exhibit distinct arcs. In the simulation, the grain capacitance, C_g was set to zero; that is, its time constant was set to zero. From the values of R_E and C_E , the estimated time constant for the electrode process,

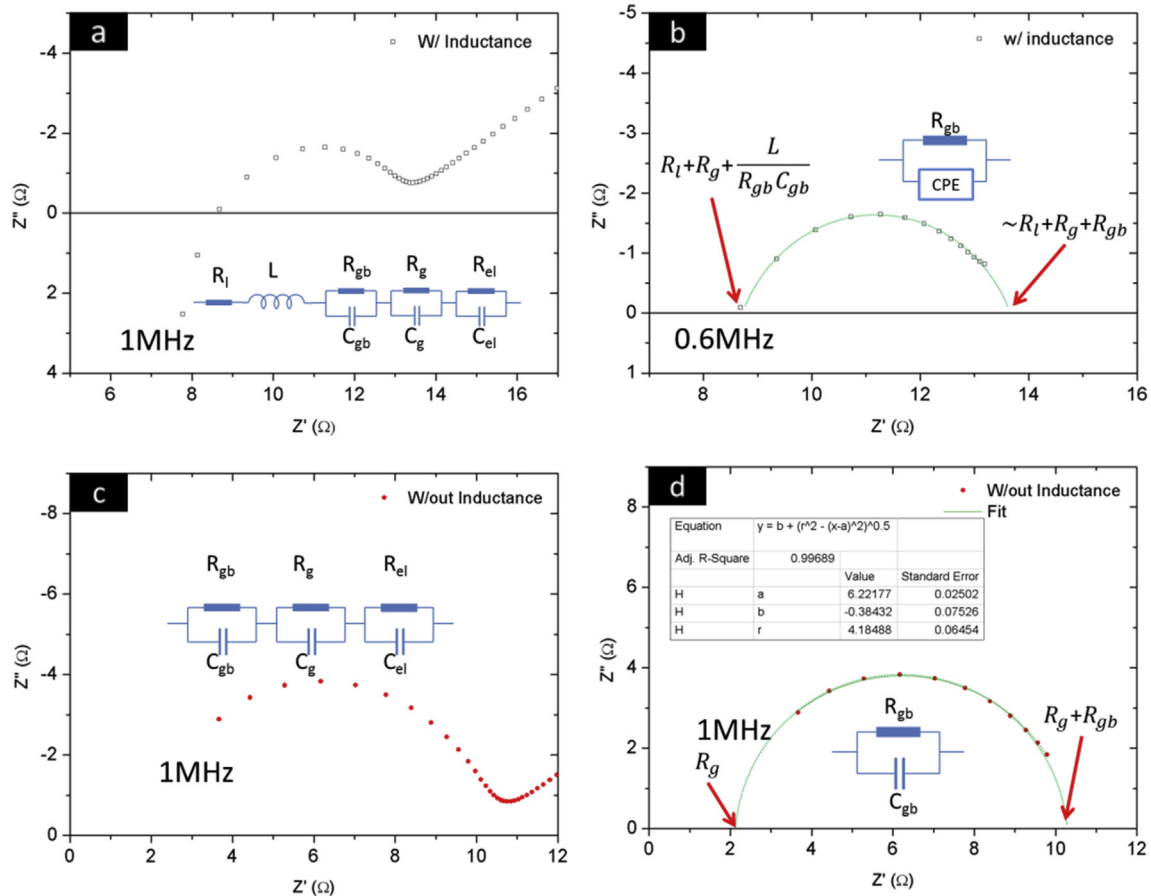


Fig. 6. Comparison between leads/instrument impedance subtraction and inductive cut-off, as well as between capacitance-fitting and CPE-fitting. (a): The high frequency regime of the measured impedance with large Pt electrodes at 600 °C. (b): The high frequency arc from (a) after cutting off the data below the x-axis. The arc is not semicircular and was fitted with a CPE. (c): The high frequency arc from (a) after subtracting the leads/instrument impedance. (d): The high frequency arc from (c). The arc could be accurately fitted as a semicircle.

$\tau_E = R_E C_E$, varies between ~ 2.12 s at 400 °C and ~ 0.59 s at 600 °C. Similarly, from the values of R_{gb} and C_{gb} , the estimated time constant for the grain boundary process, $\tau_{gb} = R_{gb} C_{gb}$, varies between $\sim 1.26 \times 10^{-5}$ s at 400 °C and $\sim 3.18 \times 10^{-7}$ s at 600 °C. Clearly, the time constants for the electrode and the grain boundary processes are sufficiently far apart which should lead to distinct arcs. This also means that the disappearance of the high frequency arc at high temperatures is not related to any overlapping spectra; but is rather related to a large contribution from the leads/instrument inductive effects.

The typical electrode thickness was about 25 microns. Also, the electrodes exhibited a sufficiently high level of porosity (typically $\sim 30\%$ based on prior work). The approximate estimate of the time constant (not strictly a time constant as the corresponding differential equation does not lead to a single time constant) for gas diffusion through the porous electrodes is estimated to be less than 0.01 s. The origin of the estimated long time constants for the electrode processes probably lies in sluggish electrode reaction of charge transfer (including adsorption, dissociation and charge transfer).

A comparison between leads/instrument impedance subtraction and inductive cutoff: The measured impedance spectra at 600 °C given in Fig. 2(b) are reproduced in Fig. 6(a) along with the equivalent circuit used for fitting (the high frequency regime). The inductive effects at high frequencies are clearly seen in the figure. In Fig. 6(b), the data below the x-axis are cutoff and an arc is fit to the

data using a CPE. Note that the arc is not semicircular, as to be expected due to the presence of inductive effects. In accord with the equivalent circuit analysis given, the high frequency intercept is given approximately by $R_l + R_g + L/R_{gb}C_{gb}$. The magnitude of the intercept from Fig. 6(b) is ~ 8.45 Ω . The magnitude of the intercept estimated using values from Table 1 is ~ 8.87 Ω showing good agreement. The low frequency intercept from Fig. 6(b) is ~ 13.95 Ω . The value of the low frequency intercept estimated from Table 1 is ~ 14.48 Ω , again showing good agreement. The arc length from the extrapolation of the data is ~ 5.5 Ω , while that based on values from Table 1 is ~ 5.61 Ω , which shows very good agreement.

Fig. 6(c) shows the high frequency data from which the measured leads/instrument impedance was subtracted. As seen in the figure, the entire spectra now lie above the x-axis. In Fig. 6(d) the high frequency part of the arc from Fig. 6(c) is reproduced, and to which a semicircular arc is fitted. Note that the arc can be fitted to a semicircle quite well. The high frequency intercept in Fig. 6(d) is identified with R_g . From Fig. 6(d), the estimated value of R_g is ~ 2.15 Ω . From Table 1, the value of R_g is ~ 2.06 Ω , showing very good agreement. The low frequency intercept in Fig. 6(d) is identified with $R_g + R_{gb}$, whose magnitude is ~ 10.3 Ω . From Table 1, the estimated value of $R_g + R_{gb}$ is ~ 10.38 Ω , again showing very good agreement. The preceding shows that after subtraction of the leads/instrument impedance, the high frequency data, which represent grain and grain boundary effects, can be well represented by a parallel $R_{gb} - C_{gb}$ circuit element.

CPE fits to low frequency data: Fig. 3(e) (650 °C) and (f) (675 °C) are reproduced respectively as Fig. 7(a) and (b). The points in black correspond to the as-measured data. The points in red correspond to the data after subtracting the leads/instrument impedance. The high frequency semicircular arcs are well resolved once the leads/instrument impedance is removed. Fig. 7(c) and (d) shows the corresponding simulated spectra in which the low frequency electrode effects are described by a CPE. The corresponding parameters are given in Table 2. As seen, the simulated spectra are in good agreement with the observed ones. However, as stated earlier, two parameters are needed for a CPE fit unlike a capacitor which requires only one. While the fits with a CPE can be well matched with the experimental data, physical interpretation is often elusive. It would appear that equivalent circuit elements that represent relevant physical/chemical phenomena are necessary. Results of fitting with a CPE are given only to demonstrate that electrode effects can be adequately fitted with a parallel CPE-resistor circuit.

Estimation of grain and grain boundary parameters using the measured spectra: In order to determine R_g , R_{gb} , and C_{gb} , the leads/instrument impedance was subtracted from the measured impedance spectra. Each of the high frequency arcs, once the leads/instrument impedance was subtracted out (Fig. 3), could be adequately described by a semicircle. In all cases, the semicircular arcs were extrapolated to the x-axis. The high frequency intercept of the semicircle corresponds to the grain resistance, R_g , and the low frequency intercept corresponds to the grain + grain boundary resistance, $R_g + R_{gb}$ [1]. The corresponding Arrhenius plots, namely, $\ln(R_g/T)$ vs. $1000/T$ and $\ln(R_{gb}/T)$ vs. $1000/T$, are shown in Fig. 8. In Fig. 8(a) and (b) first the raw data are shown on Arrhenius plots,

Table 2

Parameters used for fitting data at 650 °C and 675 °C from Fig. 3 using a CPE for the low frequency arc. The corresponding CPE fits to the data are shown in Fig. 7(a) and (b).

T	L	R_l	R_g	R_{gb}	Re	C_{gb}	CPE-T	CPE-P
650	8.58E-7	4.2	2.16	3.4	35.99	6.62E-8	9.4E-3	0.48
675	8.57E-7	4.25	2.28	1.88	22.24	1.2E-7	0.01	0.51

from which the leads/instrument impedance was not subtracted out. The data exhibit a linear behavior on the Arrhenius plots only up to a temperature of ~500 °C. Above 500 °C, the high frequency arc is not clearly resolved in the impedance spectra. This reflects as an apparent deviation from the linear behavior on the Arrhenius plots and the corresponding error is ~8 Ω. It is to be noted that the non-removal of the leads/instrument impedance means that despite Arrhenius-like behavior below 500 °C, the measured activation energies likely contain errors related to the non-removal of the leads/instrument impedance.

Fig. 8(c) and (d) shows the same data after subtracting the leads/instrument impedance. The linear behavior on Arrhenius plots is now preserved up to a temperature of 600 °C and the corresponding error level is reduced to ~2 Ω. The data shown in Fig. 8(a) through (d) were obtained on a sample with large platinum electrodes (15.8 mm diameter) and with platinum leads. Finally, Fig. 8(e) and (f) shows data obtained using small platinum electrodes (4.8 mm diameter) and with silver leads, after subtracting out the leads/instrument impedance. The linear behavior is now observed up to ~675 °C and the error level is further reduced to ~6 Ω. It is to be noted that on a relative basis an error of 6 Ω with

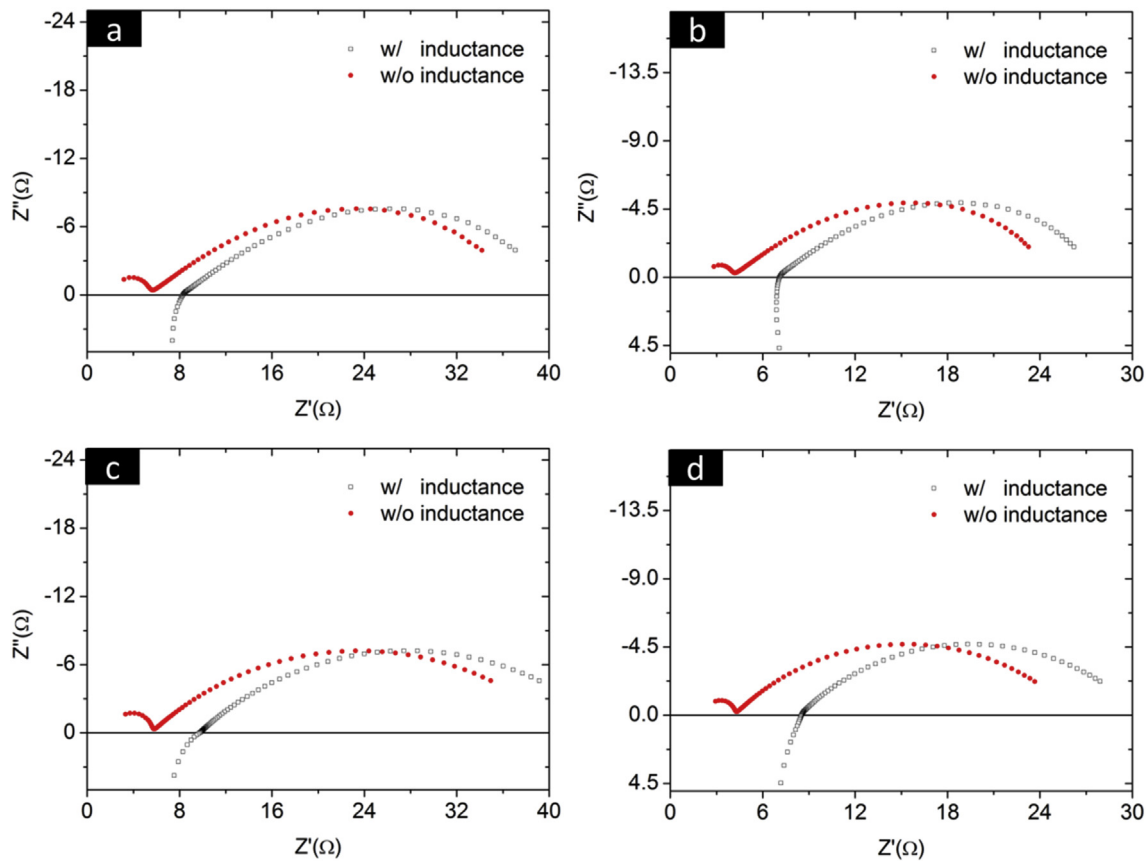


Fig. 7. EIS spectra at 650 °C and 675 °C. (a) 650 °C measured spectra and after subtracting the leads/instrument impedance. (b) 675 °C measured spectra and after subtracting the leads/instrument impedance. (c) 650 °C simulated spectra (with a CPE) with and without the leads/instrument impedance. (d) 650 °C simulated spectra (with a CPE) with and without the leads/instrument impedance.

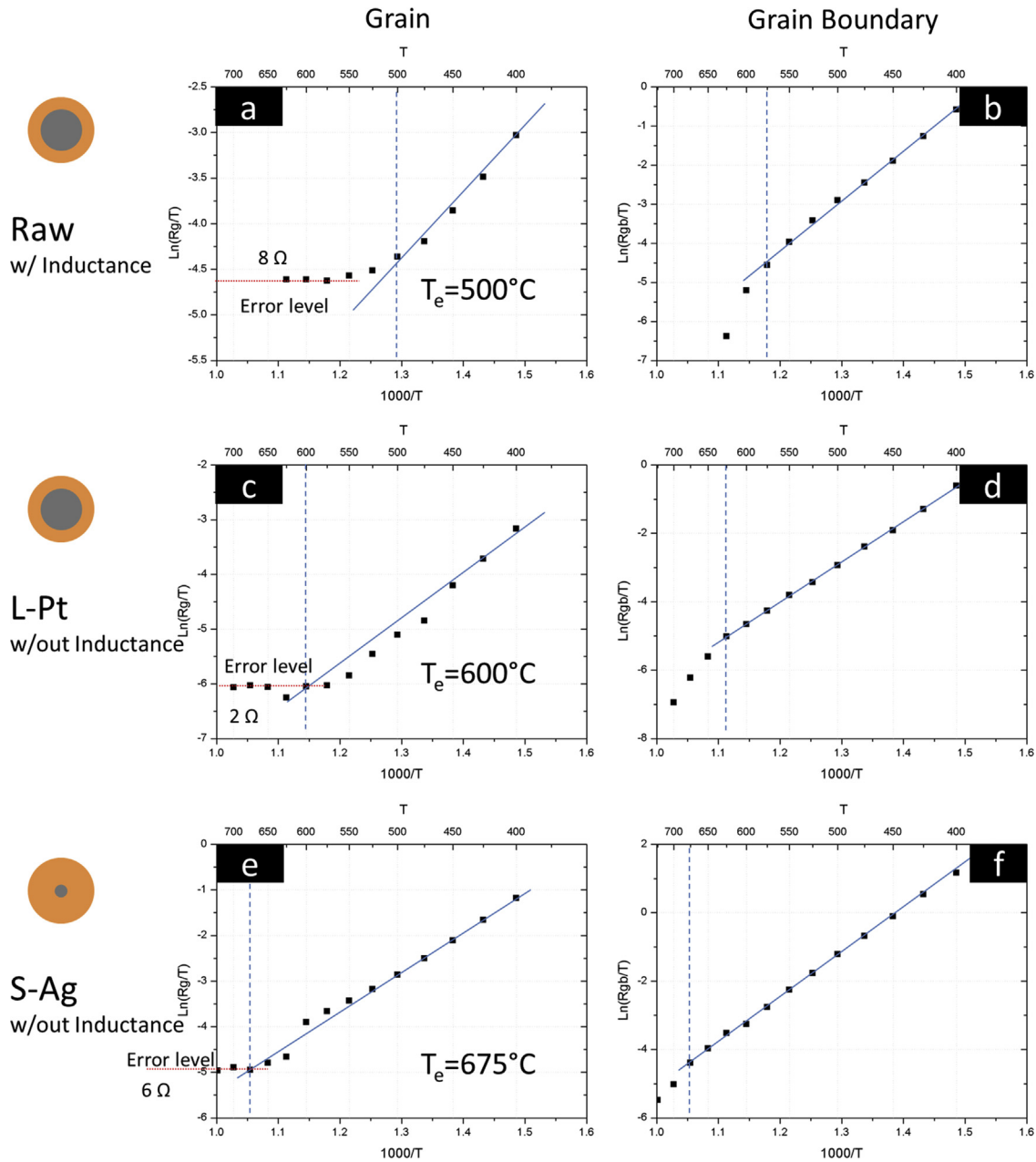


Fig. 8. Arrhenius plots corresponding to $\ln(R_g/T)$ vs. $1000/T$ (a, c, e) and $\ln(R_{gb}/T)$ vs. $1000/T$ (b, d, f) where R_g is the grain resistance and R_{gb} is the grain boundary resistance. (a) and (b) correspond to the intercepts obtained with large Pt electrodes and Pt leads without subtracting the leads/instrument impedance. (c) and (d) correspond to the intercepts obtained using data from (a) and (b) but after subtracting the leads/instrument impedance. (e) and (f) correspond to the intercepts obtained with small Pt electrodes and Ag leads after subtracting the leads/instrument impedance.

smaller electrodes is actually lower than an error of 2 Ω with larger electrodes. The present results thus show that by a suitable choice of a sample geometry and subtracting the leads/instrument impedance, the high frequency arc could be recovered and could be fitted well to a semicircle consistent with the description of the grain boundary effects using a resistor and a capacitor, as originally shown by Bauerle in his landmark paper [1]. It should be further possible to choose a sample of an appropriate geometry to increase its resistance relative to the leads/instrument impedance and extend the linear regime of the Arrhenius plots to even higher temperatures.

The data from Fig. 8(a), (c) and (e) can be fitted to [1]

$$R_g = R_g^0 T \exp\left(\frac{Q_g}{k_B T}\right) \quad (24)$$

for describing the temperature dependence of the grain resistance with R_g^0 as the pre-exponent (units of ΩK^{-1}) and Q_g as the activation energy. Similarly, data from Fig. 8(b), (d) and (f) can be fitted to

$$R_{gb} = R_{gb}^0 T \exp\left(\frac{Q_{gb}}{k_B T}\right) \quad (25)$$

for describing the temperature dependence of the grain boundary resistance with R_{gb}^0 as the pre-exponent (units of ΩK^{-1}) and Q_{gb} as

Table 3

Activation energies for transport across grain and grain boundaries of the GDC samples used in the present study. Measured activation energies are compared with literature data (Ref. [13]).

	Q_g (eV)	Q_{gb} (eV)
Raw	0.67	1.05
L-Pt	0.73	1.01
L-Ag	0.7	1.03
S-Ag	0.69	1.11
Literature [13]	0.78	0.8–1

the activation energy. The corresponding activation energies are listed in Table 3. The data obtained with small electrodes and silver wires correspond to the largest linear range on the Arrhenius plots. For the sample with large electrodes (Fig. 8(c) and (d)), the corresponding values were estimated to be: $R_g^0 = 1.2275 \times 10^{-7} \Omega \text{ K}^{-1}$ and $Q_g = 0.73 \text{ eV}$ for the grain resistance and $R_{gb}^0 = 1.3684 \times 10^{-8} \Omega \text{ K}^{-1}$ and $Q_{gb} = 1.01 \text{ eV}$ for the grain boundary resistance. For the sample with small electrodes (Fig. 8(e) and (f)), the corresponding values were estimated to be: $R_g^0 = 2.0148 \times 10^{-6} \Omega \text{ K}^{-1}$ and $Q_g = 0.69 \text{ eV}$ for the grain resistance and $R_{gb}^0 = 1.5741 \times 10^{-8} \Omega \text{ K}^{-1}$ and $Q_{gb} = 1.11 \text{ eV}$ for the grain boundary resistance. The measured activation energies are compared with literature values in Table 3 [13]. The values of the activation energies determined in the present work from samples with small electrodes, namely $Q_g = 0.69 \text{ eV}$ and $Q_{gb} = 1.11 \text{ eV}$, are deemed more accurate than those measured using larger electrodes.

From Equations (24) and (25), one may estimate grain and grain boundary resistances of the samples at other temperatures. At 800 °C, the estimated values of the grain resistance (small electrodes) is 3.764 Ω and that of the grain boundary resistance is 2.762 Ω . Thus, approximately ~58% of the resistance at 800 °C is attributed to the grain resistance and ~42% of the resistance is attributed to the grain boundary resistance. At lower temperatures, the contribution of the grain boundary resistance will be even greater. Thus, the present work shows that in order to lower the electrolyte resistance, it is necessary to reduce the grain boundary contribution. The main contributors to grain boundary resistance are the grain size (the smaller the grain size, the higher is the grain boundary contribution to the total resistance), possible impurities at grain boundaries and space charge effects. Note that the sample grain size in the present work was rather small, ~1.1 μm .

From the high frequency semicircle, the grain boundary capacitance can be obtained from the maximum in $-\text{Im } z(\omega)$. This is given by [1]

$$C_{gb} = \frac{1}{\omega_m R_{gb}} \quad (26)$$

where ω_m is the angular frequency at which $-\text{Im } z(\omega)$ is a maximum.

The C_{gb} determined using the data obtained with Pt leads with large Pt electrodes and Ag leads with small Pt electrodes are plotted in Fig. 9 vs. the measurement temperature. The data obtained with large electrodes show an increase with increasing temperature above about 600 °C. This, however, is attributed to errors associated with the incomplete removal of the leads/instrument impedance which results in significant errors in resolving the spectra at higher temperatures for the aforementioned reasons. The data obtained with small electrodes, however, show that the measured grain boundary capacitance is essentially independent of temperature over the range of temperatures over which data were obtained. This is consistent with expectations in that the grain boundary capacitance is likely determined by the grain boundary structure and chemistry [9–12], which is virtually frozen in at low temperatures over which the measurements were made. Figs. 8 and 9 respectively give absolute

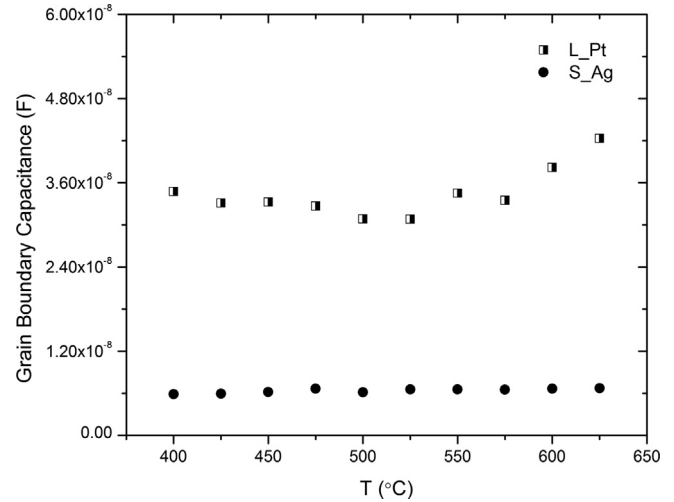


Fig. 9. Grain boundary capacitance, C_{gb} obtained by fitting to the high frequency semicircle. L_Pt corresponds to the sample with large electrodes and measured using Pt leads; S_Ag corresponds to the sample with small Pt electrodes and measured using Ag leads.

values of R_g & R_{gb} and C_{gb} instead of area specific values. The difference in the capacitance values for electrodes of smaller and larger diameters are in part due to the sizes of the electrodes. There is also an edge effect, because of which neither the capacitance nor the resistance values scale exactly with the form factors (ratio of the electrode area to the sample thickness) of the electrodes.

4. Summary

EIS measurements were made on GDC disc-shaped samples with Pt electrodes of two different sizes; 4.8 mm in diameter and 15.8 mm diameter. Measurements were made over a range of temperatures between 400 °C and 675 °C in 25° intervals. Above ~500 °C, the high frequency spectra of the samples appeared to be flattened semicircles. At 650 °C and 675 °C, no high frequency arcs were observed. Also, a significant portion of the measured impedance at high frequencies was below the x-axis consistent with a significant contribution from the leads/instrument inductance. The leads/instrument impedance was separately measured by shorting the lead wires without the sample. Once the lead impedance was subtracted from the measured total (sample + leads/instrument) impedance, the high frequency arcs could be recovered at the highest measurement temperature of 675 °C. Also, the arcs could be fitted accurately with a semicircle in each case, consistent with the corresponding equivalent circuit being a resistor and a capacitor in parallel corresponding to transport across the grain boundaries. From the measurements, after subtracting the leads/instrument impedance, the grain resistance, R_g , the grain boundary resistance, R_{gb} , and the grain boundary capacitance, C_{gb} , could be resolved. The grain resistance and the grain boundary resistance exhibited thermally activated behavior with the corresponding activation energies of $Q_g \cong 0.69 \text{ eV}$ and $Q_{gb} \cong 1.11 \text{ eV}$, respectively. The grain boundary capacitance was essentially independent of temperature. The present work underscores the importance of subtracting the leads/instrument impedance, in accord with some earlier studies [2–4]. Once the leads/instrument impedance is subtracted out, the high frequency arc could be accurately fitted with a capacitor (one parameter) and a resistor, and it was not necessary to use a CPE (which requires two fitting parameters).

The as-measured spectra were also fitted to a simple equivalent circuit in which grain, grain boundary, and electrode effects were

represented by parallel $R-C$ circuit elements. The representation of the electrode effects by a parallel $R-C$ circuit is an over simplification. Nevertheless, many salient features of the observed spectra could be deduced by analyzing maxima of the $-\text{Im } z(\omega)$ vs. $\text{Re } z(\omega)$ plots as well as minima of the $-\text{Im } z(\omega)$ vs. $\text{Re } z(\omega)$ plots. It was shown that from the minima in $-\text{Im } z(\omega)$ vs. $\text{Re } z(\omega)$ plots, one can obtain parameters representing the equivalent circuit. Thus, in cases in which the experimental range is not sufficient to estimate the parameters from the maxima and the intercepts, such as for example R_E and C_E , approximate estimates may be obtained from the minima. The present work also shows that an apparent disappearance of the grain boundary arc in measured EIS spectra at high frequencies is likely the result of not having removed the leads/instrument impedance and cannot always be interpreted to mean that the grain boundary resistance is negligible in relation to the grain resistance.

Acknowledgments

This work was supported at the University of Utah and the University of South Carolina in part by the US Department of Energy under its Energy Frontier Research Centers (EFRC) program under

Grant Number DE-SC0001061, to the University of South Carolina, HeteroFoam Center (Modeling). Part of this work was also supported at the University of Utah by Savannah River National Lab under subcontract number AC72315-O (Sample Fabrication and Electrochemical Impedance Spectroscopy).

References

- [1] J.E. Bauerle, *J. Phys. Chem. Solids* 30 (1969) 2657.
- [2] E. Barsoukov, J.R. Macdonald, *Impedance Spectroscopy: Theory, Experiment, and Applications*, Wiley-Interscience, 2005.
- [3] A. Esquirol, N.P. Brandon, J.A. Kilner, M. Mogensen, *J. Electrochem. Soc.* 151 (11) (2004) A1847–A1855.
- [4] A. Samson, M. Sogaard, R. Knibbe, N. Bonanos, *J. Electrochem. Soc.* 158 (6) (2011) B650–B659.
- [5] T. Suzuki, B. Liang, T. Yamaguchi, H. Sumi, K. Hamamoto, Y. Fujishiro, *J. Power Sources* 199 (2012) 170.
- [6] J. Wang, Y. Zhang, T. Liang, C. Deng, J. Xu, *J. Power Sources* 208 (2012) 415.
- [7] W. Zajac, J. Molenda, *Solid State Ionics* 192 (2011) 163.
- [8] W. Zajac, J. Molenda, *Solid State Ionics* 179 (2008) 154.
- [9] K. Lehovec, *J. Chem. Phys.* 21 (7) (1953) 1123–1128.
- [10] K.L. Kliewer, J.S. Koehler, *Phys. Rev.* 140 (4A) (1965) A1226–AA1240.
- [11] X. Guo, J. Maier, *J. Electrochem. Soc.* 148 (3) (2001) E121–E126.
- [12] X. Guo, W. Sigle, J. Maier, *J. Am. Ceram. Soc.* 86 (1) (2003) 77–87.
- [13] B.C.H. Steele, *Solid State Ionics* 129 (2000) 95.